PNAS RESEARCH ARTICLE | APPLIED PHYSICAL SCIENCES
APPLIED BIOLOGICAL SCIENCES

Compressibility and porosity modulate the mechanical properties of giant gas vesicles

Hedar H. Al-Terke[a,1], Grégory Beaune[a,1], Muhammad Junaid[a], Jani Seitsonen[a], Arja Paananen[b], Jaakko V. I. Timonen[a], Jussi Joensuu[b], Françoise Brochard-Wyart[c,2], and Robin H. A. Ras[a,d,2]

Edited by David Weitz, Harvard University, Cambridge, MA; received July 5, 2022; accepted December 18, 2022

Gas vesicles used as contrast agents for noninvasive ultrasound imaging must be formulated to be stable, and their mechanical properties must be assessed. We report here the formation of perfluoro-*n*-butane microbubbles coated with surface-active proteins that are produced by filamentous fungi (hydrophobin HFBI from *Trichoderma reesei*). Using pendant drop and pipette aspiration techniques, we show that these giant gas vesicles behave like glassy polymersomes, and we discover novel gas extraction regimes. We develop a model to analyze the micropipette aspiration of these compressible gas vesicles and compare them to incompressible liquid-filled vesicles. We introduce a sealing parameter to characterize the leakage of gas under aspiration through the pores of the protein coating. Utilizing this model, we can determine the elastic dilatation modulus, surface viscosity, and porosity of the membrane. These results demonstrate the engineering potential of protein-coated bubbles for echogenic and therapeutic applications and extend the use of the pipette aspiration technique to compressible and porous systems.

gas vesicles | bubbles | viscoelasticity | compressibility | porosity

Significance

Gas vesicles are produced in bacteria to achieve cellular buoyancy. These air-filled protein structures were the inspiration for developing a similar system to serve as contrast agents for ultrasound imaging. To characterize their mechanical properties, we study here the micropipette aspiration of giant gas vesicles formed by coating microbubbles with surface-active proteins adsorbed on their surface. We observe a variety of behaviors, such as large or remanent deformations. We extend current theoretical models of vesicle suction to compressible gas-filled systems and introduce the measurement of bubble permeability with this technique. We highlight the possibility of using engineered bubbles for echogenic applications and therapeutic techniques.

Gas vesicles (GV) that are produced in bacteria to achieve cellular buoyancy have opened new avenues in medicine, both for medical imaging and tumor treatment. They are air-filled protein nanostructures, hundreds of nanometers in size, which have been genetically encoded in cells and bacteria to serve as contrast agents for ultrasound imaging and as cell-killing agents by inertia-induced cavitation (1). If small unilamellar vesicles are used for drug delivery, all experiments to investigate the physics of membranes have been performed using giant unilamellar vesicles. Similarly, we study here the mechanical properties of giant gas vesicles (GGV) of sizes ranging from 10 to about 100 microns, formed by coating microbubbles with surface-active proteins adsorbed on their surface.

Ultrasound imaging is a well-established diagnostic method, and its use has grown rapidly over the past few decades due to several advantages, such as its safety, portability, real-time imaging capability, and cost efficiency (2). It has become the second most commonly used method after X-ray imaging (3). Ultrasound imaging is based on the exposure of a body to high-frequency sound waves, which are reflected at different interfaces. By calculating the propagating time and amplitude of the reflected wave (echo), an image can be constructed (4). As a mechanical wave, the echo of the ultrasound wave mainly depends on the physical properties of the medium and interfaces. To create a clear image using ultrasound, there should be clear differences in the mechanical properties between the investigated body parts. This could be achieved by using ultrasound enhanced contrast agents (UECA), which are substances with predesigned mechanical properties, mainly micro and nano-GV (5, 6).

Currently, GV play a fundamental role in therapeutic techniques and diagnosis. They can be used as drug or oxygen cargo in therapy and as contrast agents in ultrasound reflection imaging (7, 8). The main challenge in the UECA development is finding the balance between the half-life of the GV and their echogenicity, which is the ability of a substance to reflect or transmit ultrasound waves to the surrounding medium (9). This balance depends on the nature of the gas core and interfacial properties of the shell. Due to their unique physical and chemical properties, perfluorocarbons (PFCs) are confidently used in medical applications for diagnostics as well as therapy. PFCs are among the most inert and stable chemicals. Therefore, perfluoro-*n*-butane gas (C_4F_{10}) is one of the most commonly used gases for injectable ultrasound contrast agents (10). Getting insight into the shell properties is of fundamental importance for developing new contrast-enhanced agents. As cargos in therapy or as contrast agents in diagnostic, GV need to be injected intravenously. In this case, they must be robust, as it leads to a significant increase in the pressure of the gas inside, the pressure being the sum of Laplace pressure and blood pressure. The stability of GV is related to the physical properties of their shell, the nature (e.g., molecular size and polarity)

Author contributions: H.H.A.-T., G.B., A.P., J.V.I.T., J.J., F.B.-W., and R.H.A.R. designed research; H.H.A.-T., G.B., M.J., J.S., and F.B.-W. performed research; H.H.A.-T., G.B., and F.B.-W. analyzed data; and H.H.A.-T., G.B., F.B.-W., and R.H.A.R. wrote the paper.

Competing interest statement: The authors have patent filings to disclose. H.H.A.-T., G.B., J.V.I.T., and R.H.A.R. are inventors on a patent application relating to this work.

This article is a PNAS Direct Submission.

[1]H.H.A.-T. and G.B. contributed equally to this work.

[2]To whom correspondence may be addressed. Email: francoise.brochard@curie.fr or robin.ras@aalto.fi.

This article contains supporting information online at https://www.pnas.org/lookup/suppl/doi:10.1073/pnas.2211509120/-/DCSupplemental.

Published January 17, 2023.

of the gas core, and the viscosity of the ambient liquid (11). On the other hand, the echogenicity of GV is highly related to the mechanical properties of the shell. For instance, bubbles stabilized with phospholipids reflect ultrasound waves better than bubbles stabilized with polymers (5, 12), yet are more fragile than protein-coated bubbles. The lysis tension ranges between 2 and 15 mN m^{-1} for liposomes (13), whereas in our case GV are subjected to tensions up to 55 mN m^{-1} without rupture.

Hydrophobins are a group of highly surface-active proteins produced by filamentous fungi. They have a common structural feature, which is a characteristic sequence of eight cysteine residues in conserved order in their primary structure (14). These cysteine residues create four disulfide bridges (S-S bond) that bind hydrophobin protein leading to a globular shape. In addition, a hydrophobin molecule can be pictured as a natural Janus nanoparticle due to its non-centrosymmetric amphiphilic structure (15). Hydrophobins are grouped into two classes: Class I and II (16). Even though both classes share the main features such as surface activity and surface adhesion, the main functional difference between them is their solubility. The aggregates of class I hydrophobins are highly insoluble in buffer solution, while class II hydrophobins aggregates dissolve more easily (17). In addition, Linder et al. have reported that there are also differences related to the interfacial structures of class II hydrophobins (18, 19) HFBI and HFBII, which are small-sized proteins (7.5 and 7.2 kDa, respectively), produced by *Trichoderma reesei* fungi (20). Even though they are produced by the same fungi and share almost the same amphiphilic structure, HFBI and HFBII have different interfacial properties. The clearest difference between these two hydrophobins is that even if both create a viscoelastic layer at gas–liquid interfaces, HFBI layers are more glassy (21). This difference in interfacial behavior is supposed to be related to the hierarchical structure of the hydrophobin film (22). Then, coating microbubbles with HFBI could lead to GV with high stability and mechanical properties.

During the last few decades, one of the most utilized methods for measuring interfacial mechanics is surface dilatational rheology based on axisymmetric drop shape analysis (ADSA) (23–25). There are various advantages that make ADSA a cornerstone technique in many laboratories doing interfacial research. In comparison with other methods, such as Langmuir trough and Wilhelmy plate, ADSA is easy to handle, needs a relatively small sample (that makes it very popular especially if the sample is expensive), and can be done in challenging experimental conditions such as high pressure and temperature. The theory and the applications of the ADSA method are explained in a number of review articles (26–28). This technique has been used previously to approximate the surface tension of HFBI films at the air/water interface. Also, the viscoelastic properties of HFBI and HFBII films and HFBII macroscopic liquid droplets have been reported using surface shear rheology (17) and ADSA (29), respectively. Still, a challenge is to find a way to measure the properties of glassy membrane-like HFBI layer stabilizing microbubble. In this study, the mechanical properties of HFBI hydrophobin layer assembled at the gas–liquid (C_4F_{10}-water) bubble interface are measured using micropipette technique as an alternative to the traditional surface dilatational rheology technique, which failed to measure the storage and loss modulus due to the glassy nature of the layer.

The pipette aspiration technique has been developed to characterize mechanical properties of GUV (13), in particular the membrane tension, the dilatation elastic modulus, and the membrane viscosity. Its use has been extended to a wide variety of soft matter objects from living systems such as single cells (30–32) or cellular aggregates (33), to artificial systems such as liposomes (13, 34–36), emulsions (37–41), or polymersomes (42, 43). The new features of the GGV studied here include that their interior is compressible and that their membrane is slightly permeable to gas, which requires the development of a new model. We started from a preexisting model used for the analysis of incompressible capsules, which is then expanded to the case of compressible porous capsules. As a result, the aspiration of GGV with a micropipette allowed us to determine not only their elastic modulus and their surface viscosity, but also their porosity. Micropipette aspiration has previously been used to measure the water porosity of liposomes (44, 45). A liposome initially in an observation chamber at low osmolarity is aspirated in a micropipette and then transferred in another one with a higher osmolarity. The tongue length of the liposome in the micropipette is monitored. Because of the osmolarity change, the reduction of the volume of the vesicle gives rise to an excess area, which is incorporated in the tube, and the length of the aspirated tongue increases. For GV, the leaking out is induced by the Laplace pressure acting on the sucked bubble.

Model of Aspiration of GGV: Role of Compressibility and Porosity

The mechanical parameters of the bubbles can be deduced from the micropipette aspiration method developed by Evans (35). A pressure difference ΔP is imposed between a liquid medium and a pipette, and the capsule penetrates the pipette forming a tongue of length L. We describe the statics and the dynamics of suction for four cases: 1) incompressible, 2) compressible, 3) porous GV (Fig. 1 *A*–*C*), and 4) ultra-rigid GV (Fig. 1 *D*–*F*).

Incompressible Vesicles

Let us first describe the classical case of an incompressible vesicle. When a suction pressure ΔP is applied, the very narrow micropipette allows us to amplify the variation of the surface, while the vesicle size is almost constant. As the penetration length L increases, the surface area A of the vesicle increases, as well as its membrane tension σ from the initial tension σ_0 at rest to a plateau value σ_e.

The increase in tension $\Delta\sigma = \sigma - \sigma_0$ is related to the increase in capsule area ΔA.

$$\Delta\sigma = E_d^* \frac{\Delta A}{A_0}, \qquad [1]$$

where E_d^* is the dilatation modulus.

The surface of the tongue $\Delta A = 2\pi R_p L$ leads to

$$\Delta\sigma = \frac{E_d^* L R_p}{2R_0^2}. \qquad [2]$$

The driving force f_M on the hatched region (Fig. 1*A*) is the sum of capillary and pressure forces

$$-f_M = 2\pi R_p \sigma - \pi R_p^2 P_i + \pi R_p^2 \left(P_e - \Delta P\right), \qquad [3]$$

where R_p is the pipette radius, P_i is the pressure inside the capsule, and P_e is the external pressure. f_M can be written as

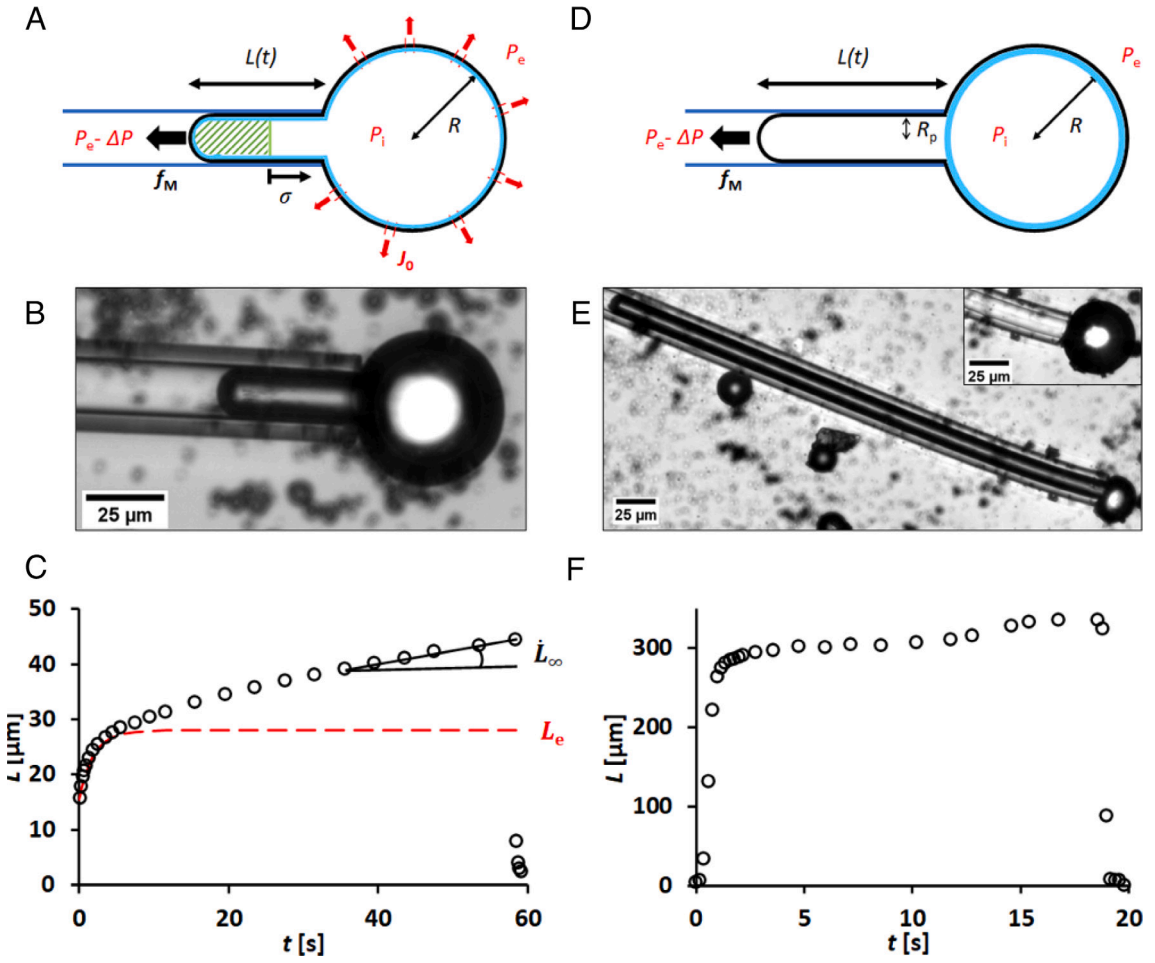

Fig. 1. Aspiration of a giant gas vesicle (*A–C*) in a liquid-like regime and (*D–F*) in a glassy regime. (*A*) Schematic of the experiment showing the geometric parameters, pressure field, and driving force f_M acting on the green hatched zone of the tongue. *L(t)* is the penetration length for $\Delta P > \Delta P_c$. The HFBI deformable coating membrane is represented by the light blue line and the bubble contour by the black line. Leak-out flows, during aspiration, through a porous membrane containing *n* pores of radius *a* (J_0 being the leak-out flow per pore), $\varphi_s \sim \frac{n a^2}{R_0^2}$ is the surface fraction of the holes. (*B*) Bright-field picture of GV aspirated in a micropipette (ΔP = 13 kPa) and (*C*) corresponding plot of the tongue length *L* as a function of time. The dashed red line is a fit using Eq. **10**, corresponding to the aspiration of a sealed capsule. The porosity of the membrane leads to a progressive deswelling, characterized by the aspiration velocity. (*D*) Schematic of the experiment of a GV with a non-deformable protein coating. (*E*) Bright-field picture of a GV aspirated in a micropipette (ΔP = 18 kPa). The inset shows the GV before aspiration (same magnification). (*F*) Corresponding plot of *L(t)* demonstrating the large and fast aspiration of the tongue in this regime.

$$f_M = \pi R_p^2 \left[\Delta P - 2\sigma\left(\frac{1}{R_p} - \frac{1}{R}\right)\right] = \pi R_p^2 \left[\Delta P - \Delta P_C - 2\Delta\sigma\left(\frac{1}{R_p} - \frac{1}{R}\right)\right], \quad [4]$$

where $\Delta P_C = 2\sigma_0\left(\frac{1}{R_p} - \frac{1}{R}\right)$ is the threshold aspiration pressure before the deformation of the protein network. Notice that this expression is valid only if *L* is larger than the pipette radius because the curvature radius of the liquid/GV meniscus involved in the Laplace law used to derive Eq. **4** is R_p.

At equilibrium, $f_M = 0$ leads to the Laplace relationship relating σ_e to ΔP, $\Delta P_C = 2\sigma_e\left(\frac{1}{R_p} - \frac{1}{R}\right)$, which can be written as

$$\Delta P - \Delta P_C = 2\Delta\sigma_e\left(\frac{1}{R_p} - \frac{1}{R}\right). \quad [5]$$

Equilibrium state of the tongue $L = L_e$

From Eqs. **2** and **5**, we get

$$\Delta\sigma_e = \frac{E_d^* L_e R_p}{2R_0^2} = \frac{\Delta P - \Delta P_C}{2\left(\frac{1}{R_p} - \frac{1}{R}\right)}.$$

Leading to

$$L_e = \frac{R_0^2}{E_d^*} \frac{\Delta P - \Delta P_C}{\left(1 - \frac{R_p}{R}\right)}. \quad [6]$$

The curve L_e versus ΔP leads to a measurement of E_d^*. Notice that Eq. **6** derived from Eq. **4** is valid only for $L > R_p$. $L = R_p$ defines a threshold aspiration pressure ΔP_c^*.

Dynamics of Penetration

When $L < L_e$, the driving force f_M is positive and is balanced by the friction force f_V(46)

$$f_V = 4\pi\eta_s \dot{L}\left(1-\frac{R_p^2}{R^2}\right), \quad [7]$$

where $\eta_s = \eta_M e$ is the surface viscosity of the membrane of thickness e.

$f_M = f_V$ leads to the dynamical equation for $L(t)$

$$\pi R_p^2\left(\Delta P-\Delta P_C\right) = \pi E_d^* \frac{R_p^2}{R^2} L\left(1-\frac{R_p}{R}\right) + 4\pi\eta_s \dot{L}\left(1-\frac{R_p}{R}\right)\left(1+\frac{R_p}{R}\right). \quad [8]$$

This equation involves a characteristic time τ_M

$$\tau_M = \frac{4\eta_s R^2}{E_d^* R_p^2}\left(1+\frac{R_p}{R}\right) \sim \frac{4\eta_s R^2}{E_d^*\ R_p^2}, \quad [9]$$

if $R_p \ll R$ and the solution $L(t)$ is given by

$$L(t) - L_i = \left(L_e - L_i\right)\left(1-e^{-\frac{t-t_0}{\tau_M}}\right), \quad [10]$$

where L_i is the initial deformation at time t_0.

Compressible GV

For a liquid droplet, the volume is conserved. For a gas bubble, the internal pressure of the gas increases as σ increases and the volume of the compressed gas decreases. For the internal gas, $P_i V = NkT$ is constant, with N the number of gas molecules and k the Boltzmann constant.

Before the GV's suction, $\Delta P = 0$ and $P_i = P_e + 2\frac{\sigma_0}{R_0}$. As the GV is sucked, $\Delta P \neq 0$, the membrane tension σ increases, and $P_i = P_e + 2\frac{\sigma}{R}$. This ideal gas law leads to $\left(P_e + 2\frac{\sigma_0}{R_0}\right)R_0^3 = \left(P_e + \frac{2\sigma}{R}\right)R^3$. Assuming $\frac{(R-R_0)}{R_0} \ll 1$, we get

$$-\frac{3\left(R-R_0\right)}{R_0} = 2\frac{\sigma-\sigma_0}{R_0 P_e}. \quad [11]$$

The compression of the gas leads to a decrease of the capsule area A, which is now given by $A = 2\pi R_p L + 4\pi R^2$.

Since $A_0 = 4\pi R_0^2$ Eq. **1** now leads to

$$\Delta\sigma = E_d^* \frac{A-A_0}{A_0} = E_d^*\left(\frac{LR_p}{2R_0^2} + 2\frac{R-R_0}{R_0}\right). \quad [12]$$

Inserting $\left(R-R_0\right)$ (Eq. 11) in Eq. 12 leads to

$$\Delta\sigma\left(1+\frac{4\ E_d^*}{3R_0P_e}\right) = \frac{E_d^*\ LR_p}{2R_0^2}. \quad [13]$$

At equilibrium, $\sigma = \sigma_e$ is given by the Laplace law $\Delta P = 2\sigma_e\left(\frac{1}{R_p}-\frac{1}{R}\right)$ and $\Delta P - \Delta P_C = 2\Delta\sigma_e\left(\frac{1}{R_p}-\frac{1}{R}\right)$. Inserting $\Delta\sigma = \Delta\sigma_e$ in Eq. 13 leads to

$$L_e = \frac{R_0^2}{E_d^*}\frac{\Delta P-\Delta P_C}{\left(1-\frac{R_p}{R}\right)}\left(1+\frac{4\ E_d^*}{3R_0P_e}\right) = \frac{R_0^2\left(\Delta P-\Delta P_C\right)}{E_{d\ eff}^*\left(1-\frac{R_p}{R}\right)}. \quad [14]$$

with $E_{d\ eff}^* = \frac{E_d^*}{1+\frac{4E_d^*}{3R_0P_e}}$.

The compression of the bubble reduces its area, leading to a more elongated tongue. The increase of L_e due to the gas compression is $\frac{\Delta L_e}{L_e} = \frac{4E_d^*}{3R_0P_e}$. This will be an important correction if E_d^* is large, which is the case of HFBI coating layers where the Laplace pressure of the bubble is comparable to the atmospheric pressure P_e. The dynamics of penetration of the compressible GV $L(t)$ is still given by Eq. **10**, with

$$\tau_M = \frac{4\eta_S R^2}{E_d^* R_p^2}\left(1+\frac{4E_d^*}{3R_0P_e}\right)\left(1+\frac{R_p}{R}\right) = \frac{4\eta_S R^2}{E_{d\ eff}^* R_p^2}\left(1+\frac{R_p}{R}\right). \quad [15]$$

Aspiration of a Porous Vesicle

As shown in Fig. 1*B*, the length of the tongue does not reach a plateau value but instead increases with time. It shows that the vesicle is permeable. In the case of a porous vesicle, the increase of the Laplace pressure $\Delta\left(P_i - P_e\right) = \frac{2\Delta\sigma}{R}$ leads to a leak-out of the internal gas. The flux J through the n pores (47) is

$$J = \frac{2na^3\Delta\sigma}{3\eta_L R}, \quad [16]$$

where η_L is the viscosity of the ambient medium and a is the radius of the pores.

If we want to determine the porosity P_M of the GV, we can write the flow J in terms of the porosity as follows

$$-\frac{dV}{dt} = J = P_M\frac{Av_0\Delta\left(P_i-P_e\right)}{kT},$$

where $P_M = \frac{na^3kT}{3\eta_L A v_0}$, with v_0 the volume of a gas molecule.

This leak-out leads to a decrease of the internal volume

$$-4\pi R^2\dot{R} = J, \quad [17]$$

While the leak-out leads to a decrease of the vesicle area $8\pi R\dot{R}$, the suction of the tongue leads to an increase $2\pi R_p\dot{L}$. The total change of the area of the vesicle per unit time is thus given by

$$\frac{dA}{dt} = 2\pi R_p\dot{L} + 8\pi R\dot{R} = 2\pi R_p\dot{L} - \frac{2J}{R} = 2\pi R_p\dot{L} - \frac{4na^3}{3\eta_L}\frac{\Delta\sigma}{R^2}. \quad [18]$$

When the stationary regime is reached $\frac{dA}{dt}=0$, σ tends to σ_∞ and $\frac{dL}{dt}$ tends to a constant $\dot{L}_\infty$. The length $L(t)$ of the tongue increases at constant velocity. $\dot{L}_\infty$ and $\Delta\sigma_\infty$ are related by

$$R_p\dot{L}_\infty=\frac{2na^3}{3\eta_L\pi}\frac{\Delta\sigma_\infty}{R^2}, \qquad [19]$$

given by Eq. **18** for $\frac{dA}{dt}=0$.

We now calculate the dynamics of suction. The insertion of $\frac{dA}{dt}$ in the derivation of $\Delta\sigma$ given by Eq. **12** leads to

$$\frac{d\Delta\sigma}{dt}=\frac{E_d^*}{A_0}\frac{dA}{dt}=\frac{E_d^*}{A_0}\left(2\pi R_p\dot{L}-\frac{4na^3}{3\eta_L}\frac{\Delta\sigma}{R^2}\right), \qquad [20]$$

with $\dot{L}=\frac{\pi R_p^2\left[\Delta P-2\sigma\left(\frac{1}{R_p}-\frac{1}{R}\right)\right]}{4\pi\eta_S\left(1-\frac{R_p^2}{R^2}\right)}=\frac{\pi R_p^2\left[\Delta P-\Delta P_C-2\Delta\sigma\left(\frac{1}{R_p}-\frac{1}{R}\right)\right]}{4\pi\eta_S\left(1-\frac{R_p^2}{R^2}\right)}$

derived from the force balance $f_M=f_V$. That leads to

$$\frac{d\Delta\sigma}{dt}=\frac{E_d^*}{A_0}\frac{2\pi^2R_p^3\left[\Delta P-\Delta P_C-2\Delta\sigma\left(\frac{1}{R_p}-\frac{1}{R}\right)\right]}{4\pi\eta_S\left(1-\frac{R_p^2}{R^2}\right)}-\frac{E_d^*}{A_0}\frac{4na^3}{3\eta_L}\frac{\Delta\sigma}{R^2}. \qquad [21]$$

The solutions $\sigma(t)$ and $R(t)$ are given by Eqs. **17** and **21** with the boundary conditions $\sigma(0)=\sigma_0$, $\Delta\sigma(0)=0$, and $R(0)=R_0$.

Considering $R\gg R_p$, Eq. **21** becomes $\frac{d\Delta\sigma}{dt}+\Delta\sigma\frac{E_d^*}{A_0}\left[\frac{\pi R_p^2}{\eta_S}+\frac{4na^3}{3\eta_LR^2}\right]=\frac{E_d^*}{A_0}\ \pi R_p^3\frac{\Delta P-\Delta P_C}{2\eta_S}$, which can be written as

$$\frac{d\Delta\sigma}{dt}+\frac{\Delta\sigma}{\tau}=\frac{E_d^*}{A_0}\ \pi R_p^3\frac{\Delta P-\Delta P_C}{2\eta_S}, \qquad [22]$$

where $\frac{1}{\tau}=\frac{1}{\tau_M}+\frac{1}{\tau_L}$, by setting $\frac{1}{\tau_M}=\frac{E_d^*\pi R_p^2}{A_0\eta_S}$, where τ_M is the viscous membrane flow relaxation time, and $\frac{1}{\tau_L}=\frac{E_d^*4na^3}{A_03\eta_LR^2}$, where τ_L is the leak-out flow relaxation time.

At short time, $R\sim R_0$ and Eq. **22** leads to $\Delta\sigma(t)=\Delta\sigma_\infty\left(1-e^{-t/\tau}\right)$ with $\Delta\sigma_\infty=\tau\frac{E_d^*}{A_0}\pi R_p^3\frac{(\Delta P-\Delta P_C)}{2\eta_S}$ and

$$\frac{1}{\tau}=\frac{E_d^*}{A_0}\left(\frac{\pi R_p^2}{\eta_S}+\frac{4na^3}{3\eta_LR_0^2}\right)=\frac{E_d^*\ \pi R_p^2}{A_0\eta_S}\left(1+\frac{1}{Q}\right), \qquad [23]$$

where Q, the sealing parameter, is defined by the ratio $Q=\frac{\tau_L}{\tau_M}$

$$Q=\frac{\pi R_p^2 3\eta_LR_0^2}{4na^3\eta_S}=\frac{3\pi R_p^2\eta_L}{4\phi_S\eta_Sa}, \qquad [24]$$

by setting $\phi_S=\frac{na^2}{R_0^2}$. We can also express Q in terms of the porosity P_M using

$$Q=\frac{R_p^2kT}{16\eta_Sv_0P_M}. \qquad [25]$$

The sealing parameter Q controls two regimes:

A) In the limit of a low porosity membrane $Q\gg1$ ($\tau_M\ll\tau_L$) and the relaxation time $\tau\simeq\tau_M$, we have a weak leak-out and $\Delta\sigma_\infty=\frac{R_p}{2}\left(\Delta P-\Delta P_C\right)$. The velocity of extrusion given by Eq. 19 is

$$\dot{L}_\infty=\frac{na^3\left(\Delta P-\Delta P_C\right)}{3\pi\eta_LR^2}=\frac{4P_Mv_0\left(\Delta P-\Delta P_C\right)}{kT}. \qquad [26]$$

B) In the limit of a highly porous membrane, $Q\ll1$ ($\tau_V\gg\tau_L$), we have a strong leak-out and $\sigma_\infty=\frac{R_p}{2}Q\left(\Delta P-\Delta P_C\right)$. This is a new regime, which could be obtained if the mesh size of the coating network is loose or for Pickering bubbles, when microparticles coat the interface.

In that case, $\tau=\tau_L=\frac{3\pi\eta_LR_0^4}{E_d^*na^3}$, and

$$\dot{L}_\infty=\frac{R_p^2\left(\Delta P-\Delta P_C\right)}{4\eta_S}. \qquad [27]$$

C) In the intermediate case, $\dot{L}_\infty$ is given by Eqs. 19 and **23**. This leads to

$$\dot{L}_\infty=\frac{Q}{1+Q}\frac{na^3\left(\Delta P-\ \Delta P_c\right)}{3\eta_L\pi R_0^2}, \qquad [28]$$

which can be written in term of porosity as

$$\dot{L}_\infty=\frac{4P_Mv_0}{kT}\ \frac{Q\left(\Delta P-\ \Delta P_c\right)}{1+Q}. \qquad [29]$$

Aspiration of Liquid Porous Compressible GV

We summarize here the results of the previous parts of the model to describe the aspiration length $L(t)$ assuming that the vesicles are in a liquid state, *i.e.*, $\Delta P>2\sigma_y/R_p$ for glassy vesicles.

A) The aspiration length tends to a plateau value if the porosity of the polymer coating is extremely low, corresponding to $Q\to\infty$

$$L_e=\frac{R_0^2}{E_d^*}\left(1+\frac{4E_d^*}{3R_0P_e}\right)\left(\Delta P-\Delta P_c\right).$$

This length $L(t)$ tends to L_e exponentially (Eq. **10**).

B) For intermediate values of Q, $\tau_M<\tau_L$, the dynamics $L(t)$ can be written as

$$L(t) - L_i = \left(L_e - L_i\right)\left(1 - e^{-\frac{t-t_0}{\tau_M}}\right) + \dot{L}_\infty t, \qquad [30]$$

where $\dot{L}_\infty$ is given by Eq. **26**.

Aspiration of Ultra-Rigid GV: Gas Extraction Regime

Glassy regimes are observed for bubbles below a radius R_0^*. Both R_0^* and the rigidity of the coating depend on the incubation time. These GV are characterized by a yield stress σ_y. If $\Delta P < \sigma_y$, the coating cannot expand and σ remains equal to the initial tension σ_0. We show here that a tongue of gas can form if $\Delta P \gtrsim \frac{2\gamma}{R_p}$, where γ is the surface tension of the medium equal to 64.5 mN m^{-1} for a glycerol solution (50% w/w in distilled water) and 72 mN m^{-1} for pure water. We study the regime $\sigma_y > \Delta P > \frac{2\gamma}{R_p}$ illustrated in Fig. 1 *D*–*F*.

In this case, σ is constant ($\sigma = \sigma_0$) and the driving force on the tongue is given by

$$f_M = \pi R_p^2 \left[\Delta P - \frac{2\gamma}{R_p} + 2\frac{\sigma_0}{R}\right].$$

As soon as $\Delta P > \frac{2\gamma}{R_p}$, a tongue of gas is formed and expands. The gas pressure decreases and may lead to a deflation of the capsule. The tongue ultimately stops when all the gas is sucked in the pipette. We have $\frac{2\gamma}{R_p} \sim 18$ kPa for $R_p = 7$ µm and $\gamma = 64.5$ mN m^{-1}.

The dynamics of the tongue is extremely fast. f_M is balanced by the friction force $f_V = 8L_t\eta_L\pi\dot{L}$, due to the viscous flow inside the pipette induced by the expansion of the tongue of gas, where L_t is the length of the micropipette and η_L the medium viscosity. It leads to

$$\dot{L} = \frac{R_p^2}{8L_t\eta_L}\left(\Delta P - \frac{2\gamma}{R_p}\right). \qquad [31]$$

Considering $R_p = 7$ µm, $\eta_L = 6.5\ 10^{-3}$ Pa s, $L_t = 1$ cm, and $\Delta P - \frac{2\gamma}{R_p} \sim 2$ kPa, it leads to an aspiration velocity $\dot{L} = 200$ µm s^{-1}. This value is in agreement with the experimental data, where the very fast aspiration of the tongue can be seen in the plot in Fig. 1*F*.

Results and Discussion

Formation of GV. The GV are produced by mechanical agitation. 15 min after their formation, a single white phase is observed. Afterward, they migrate according to their size and we observe the formation of a very diffuse layer on the top containing the larger GV, while the rest of the sample, less diffusive and opaque, contains the smaller ones (*SI Appendix*, Fig. S1).

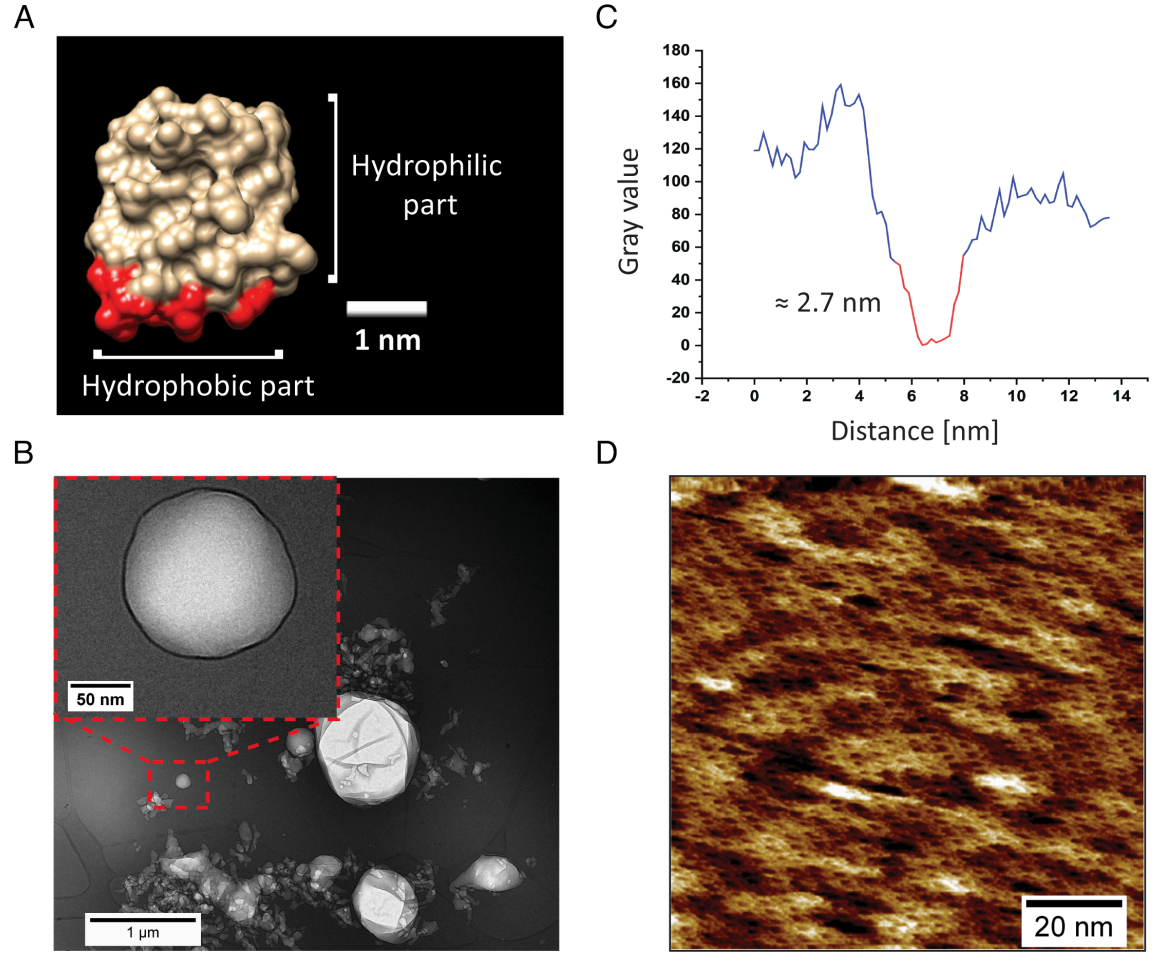

Fig. 2. Structure of the protein coating at the gas–liquid interface of GV. (*A*) 3D structure of an HFBI protein. The yellow color shows the hydrophilic part, and the red color shows the hydrophobic part (PDB ID 2FZ6, image created using Chimera software, version chimera 1.15). (*B*) Cryo-TEM image of GV consisting of C_4F_{10} stabilized with HFBI. (*C*) Thickness of the shell measured from the cryo-TEM images using ImageJ software. (*D*) AFM image of an HFBI layer at the air–water interface. This image shows the crystalline structure and the porosity of the film [the large dark areas could be sample defects, while the small dark areas represent the areas between the HFBI molecules (pores)].

Structure of GV. Due to its amphiphilic nature (Fig. 2*A*) and its high affinity to self-assemble at hydrophobic–hydrophilic interfaces, HFBI creates an amphiphilic shell around C_4F_{10} bubbles, resulting in spherical GV of nanometer to micrometer size (*SI Appendix*, Fig. S1). The structure of these GV studied by Cryotransmission Electron Microscopy (cryo-TEM) (Fig. 2*B*) shows that for all sizes encountered (up to 1 μm), the membrane thickness is 2.7 ± 0.4 nm (n = 8, Fig. 2*C*). As this value is comparable to the size of an HFBI protein (21), we can deduce that the bubbles are covered by a protein monolayer. We are not able to measure larger GV by cryo-TEM, but we assume that their membrane thickness also corresponds to a protein monolayer.

The Atomic Force Microscopy (AFM) image of the HFBI layer at the air/water interface (Fig. 2*D*) shows a crystalline arrangement of HFBI molecules with a regular roughly hexagonal pattern of holes. These nanosized holes represent the structural porosity of the shell. The large dark areas in the image are empty and most probably are sample preparation defects. The layer structure in this image matches the structure reported in the literature (21, 22). Even though the molecular size and polarity of C_4F_{10} and air differ, we assume that the HFBI layer structure could be the same because both gases are hydrophobic.

Surface Tension σ_0 of GV. A non-polar gas bubble (C_4F_{10}) is initiated on the tip of a hooked needle inside a solution consisting of 0.01 mg mL^{-1} of HFBI (Fig. 3). The surface tension versus time plot shows the three phases of the self-assembly process. First, the HFBI molecules diffuse to the bubble surface. Second, the molecules adsorb at the interface, and lastly, the surface reaches the saturation state, whose surface tension value represents the static surface tension of the HFBI solution at the gas surface. The value is about σ_0 = 55 mN m^{-1}, which is significantly lower than the surface tension of pure water (72 mN m^{-1}). It means that we have a layer of HFBI adsorbed at the interface. Also, the figure shows that at the end of the surface tension curve, there is some increase in the surface tension value. This phenomenon does not indicate a true increase but is rather due to a misfitting of the Laplace equation, as the software was not able to calculate the correct value of the surface tension. The best interpretation of this case is that a quite rigid HFBI layer is formed, which does not obey the liquid properties required by the Laplace equation. Furthermore, when sinusoidal volume changes were applied on the same GV, the software failed to measure the mechanical properties of the layer. As shown in *SI Appendix*, Fig. S3, the volume curve does not fit the surface tension curve and has some values that are not correct. Therefore, finding an alternative method to measure the mechanical properties of the protein layer represents a fundamental priority to complete this study and any similar future works related to self-assembled rigid layers.

For comparison, surface tensions ranging from 30 mN m^{-1} to 50 mN m^{-1} were found performing equilibrium surface tensiometry experiments for similar HFBI concentrations (17) and shape analysis of deflated capsules (29). Also, the determination of the surface tension for high concentrations has to be taken with caution due to the formation of the glassy film of HFBI (17). The difficulty in determining the surface tension of HFBI layers is confirmed by Szilvay et al. (21) who failed to determine it using the ADSA method due to the unexpected deformation of the drops. Details about the ADSA method can be found in *SI Appendix*, Fig. S4.

Micropipette Aspiration of GV. To study the elastic and viscous properties of the GV, we use the micropipette aspiration technique. The details of all the main parameters determined and calculated for the experiments performed in distilled water are given in *SI Appendix*, Table S1.

As we will see, it is necessary to apply high pressures to aspirate these GV. It is then cumbersome to use a classical pipette setup in which the pressure is controlled by modifying the height between the observation chamber and the water reservoir. Instead, we use here a piezoelectric pressure controller allowing to easily exceed 10 kPa, otherwise requiring classically a displacement of the water tank higher than 1 m.

GV range in size from the nanoscale to the micrometer scale. Since we are limited by the minimum radius of the micropipettes that can be prepared, we consider GV with $R \geq 15$ μm when their

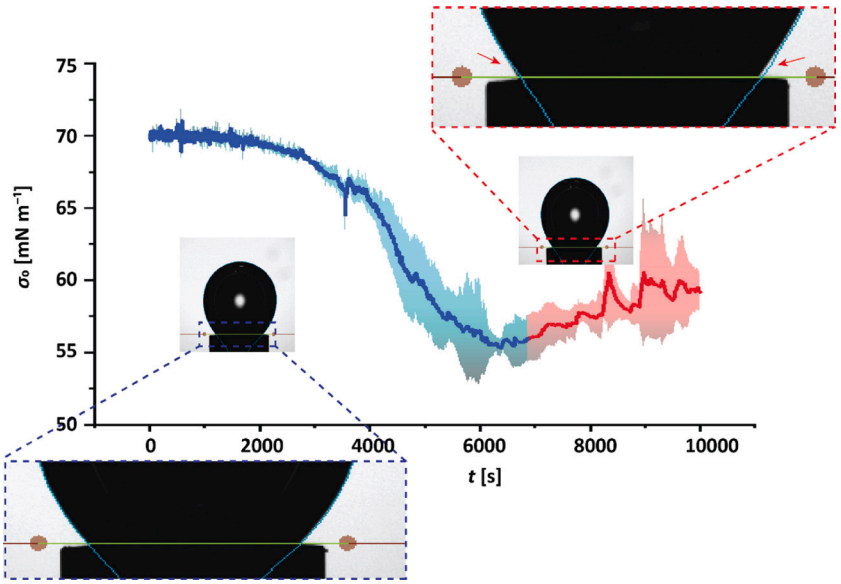

Fig. 3. Surface tension development of HFBI at the liquid–gas (C_4F_{10}) interface. The blue part of the curve shows the regime where the software fits the GV shape. As shown in the magnified image below the curve, the fit line (light blue) matches the bubble shape perfectly (black area above the green line). In contrast, the red part shows the regime for which the software could not fit the GV shape. The magnified image above the red curve shows the mismatch between the fit line (light blue) and the bubble shape, the mismatched areas being indicated by two red arrows. This leads to an incorrect determination of the surface tension value.

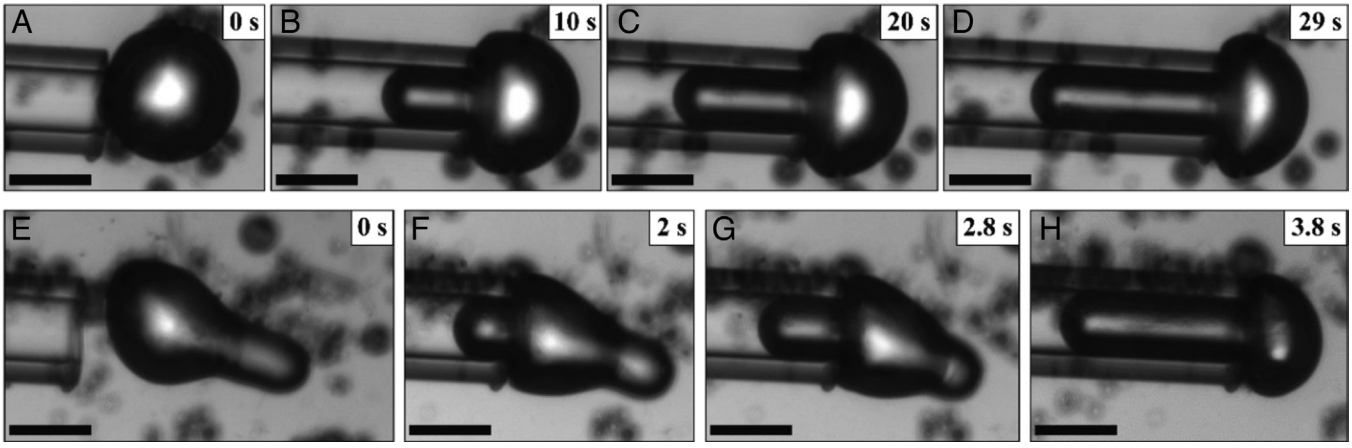

Fig. 4. Solid-like behavior of GV. (*A–D*) Snapshots at different times of aspiration with ΔP = 14.5 kPa revealing the glassy behavior of an HFBI-coated microbubble aspirated into a micropipette. While the GV is aspirated in the micropipette, the outer part is less spherical. (*E–H*) Glassy behavior of an HFBI-coated microbubble. (*E*) The microbubble released after aspiration exhibits a remanent deformation. (*F–H*) Aspiration of the GV with ΔP = 13.5 kPa from the other side at different times, leading to the decrease of the free tongue length. It demonstrates that the stress is larger than the yield above which the solid becomes a liquid. (Scale bars, 20 μm.)

dynamics of aspiration is studied, and $R \geq 10$ μm when only the observation of their behavior is needed (i.e., without parameter determination). We apply a pressure ΔP between 12 and 20 kPa, which is extremely large $\left(\frac{\Delta P}{P_e} \sim 0.1 - 0.2\right)$, meaning that the gas compression will be an important factor.

We aspirate a GV for about 10 to 60 s so that the length of the tongue in the pipette is at least 3 times the pipette radius (Fig. 4 *A–D*). The parameters are chosen individually for each GV to apply sufficient pressure to aspirate the vesicles and sufficient time so that we observe both the initial elastic deformation followed by a steady flow in the pipette. As the GV is aspirated, its shape becomes less and less spherical. At that point, we stop the applied pressure and observe two types of behavior: either a liquid-like behavior where the tongue retracts completely, and the bubble recovers completely with spherical shape as before the aspiration (Movie S1) or a glassy behavior (Movie S2) where the tongue does not relax and retains the sleeve shape, while the vesicle keeps a pear-like shape (Fig. 4*E* and Movie S3). The tongue remains permanent after expulsion from the pipette (Movie S4). The phase diagram liquid versus glassy as a function of the size and aging times of GV is shown in *SI Appendix*, Fig. S6. The liquid-like behavior is observed for "young" and large GV, whereas the solid-like behavior for small and mature GV.

We also successively aspirated the GV, changing the position of the micropipette on the surface of the same vesicles between several consecutive aspirations. For liquid-like GV that showed no deformation during the first aspiration (Movie S1), there was still no change after several successive aspirations. On the other hand, for the more rigid GV that were moderately deformed after the first aspiration, the deformation is increasingly pronounced. Finally, for glassy GV with a strong remanent deformation after the first aspiration, we observe the aspiration of a new tongue accompanied simultaneously by the retraction of the first one (Fig. 4 *E–H* and Movie S5). This feature has also been observed for glassy lipid vesicles and glassy polymersomes, which flow above a threshold pressure named the yield stress (42). The remanent deformation disappears when we apply a pressure higher than the yield stress, which ranges from 8.1 to 13.1 kPa, n = 8, with a mean value 10.5 kPa.

These behaviors differ greatly from what we would have obtained with uncoated bubbles. They would have been completely aspirated as soon as ΔP is larger than a critical pressure $\Delta P_C = 2\gamma\left(\frac{1}{R_p} - \frac{1}{R}\right)$ (Movie S6), related to the surface tension γ of the liquid, which is constant. In the presence of the hydrophobin coating of the bubbles, γ is replaced by the membrane tension σ, which increases when the vesicle is sucked into the pipette.

To interpret the role of bubble size in the liquid-like or glassy behavior of GV, we postulate that this transition is a result of the larger vesicles needing more time to reach the saturated state of the adsorbed layer. If we assume that the proteins are deposited by diffusion, at a time t the proteins in a volume $(Dt)^{\frac{3}{2}}$ will cover the surface area $4\pi R_0^2$ of the bubble, where D is the diffusion coefficient of the proteins. This simple argument shows that the equilibrium coating time t_e, given by $\left(Dt_e\right)^{3/2} c = 4\pi R_0^2 c_s$ is proportional to $R_0^{\frac{4}{3}}$ and is shorter for smaller vesicles. In the phase diagram representing liquid versus glassy behavior for GV of different radii versus time, we should be able to fit the coexistence curve using the following equation

$$R_0^* = D^{\frac{3}{4}} c^{\frac{1}{2}} c_S^{-\frac{1}{2}} t^{\frac{3}{4}}, \qquad [32]$$

where c is the initial protein concentration and c_S is the protein density of the shell at saturation.

To test this model, we study R_0^* versus c for different initial protein concentrations (0.2, 0.067, and 0.02 mg mL^{-1}). We set t = 0 the time when the bubbles are prepared, and we first consider c = 0.2 mg mL^{-1} (Fig. 5). During the first 3 h after their formation, all GV, regardless of their size (within the low size limit that can be aspirated with the micropipettes), show no deformation after aspiration. Between 3 and 7 h, the smallest aspirated vesicles show persistent deformation, and then the GV that remain deformed are increasingly larger, with a radius of up to 20 μm. At longer times, persistent deformation of much larger GV is observed, for example with radii up to 100 μm after 3 d (*SI Appendix*, Fig. S5). Approximating a value of $c_S = a_0^{-1}$, where a_0 is the surface area per protein of order 9 nm^2, $c_S = 10^{17}$ molecules per m^2, the fit of Eq. **30** leads to $D^{3/4} c^{1/2} c_S^{-1/2} = 1.2\ 10^{-8}$ ms$^{-¾}$. We can deduce a diffusion coefficient $D \sim 10^{-14}$ m^2 s^{-1}. By performing similar

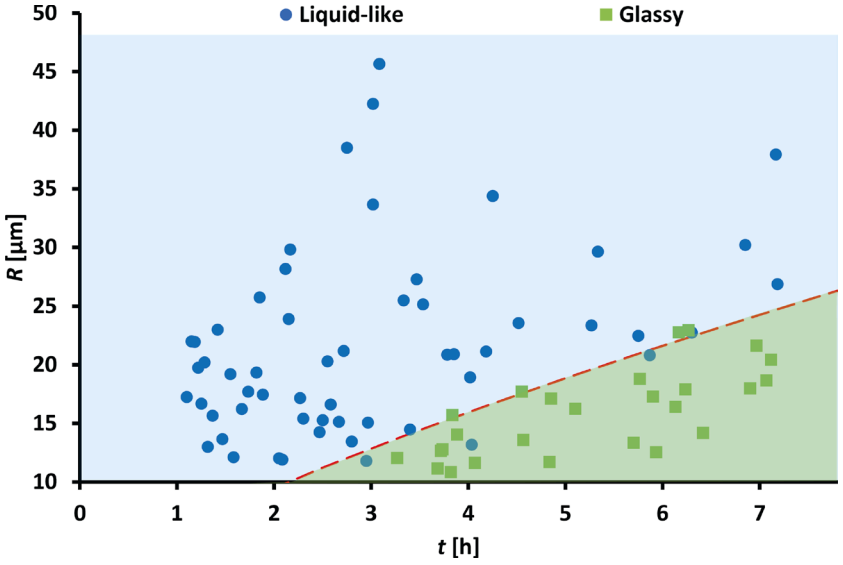

Fig. 5. Behavior of the aspirated GV over time (n = 83). Either they show a liquid-like behavior (no apparent deformation, blue dots, and area), or a glassy behavior (they remain deformed, green rectangles, and area). The brown-dashed line corresponds to the fit Eq. **30**.

experiments with lower initial protein concentrations, the transition is still observed but is shifted toward long times and for smaller GV as c decreases (*SI Appendix*, Fig. S6). For c = 0.067 and 0.02 mg mL^{-1}, we find, respectively, $D^{3/4}c^{1/2}c_S^{-1/2}$ = 1.1 10^{-8} and 9.5 10^{-9}, which is in agreement with the scaling relationship for R_0^* versus c.

Using the model developed in the theoretical part, we can analyze the data to determine the mechanical properties of the GV. We plot the aspiration length of the tongue inside the pipette over time. Upon application of suction pressure ΔP, we observe a rapid increase in length during the first few seconds corresponding to the regime described by Eq. **10** that is followed by a penetration at constant velocity $\dot{L}_\infty$ due to the permeability of the porous membrane, leading to the leakage of gas molecules. The data can be fitted with Eq. **30** $L(t) - L_i = \left(L_e - L_i\right)\left(1 - e^{-\frac{t-t_0}{\tau_M}}\right) + \dot{L}_\infty\, t$, with L_i the initial tongue length, L_e the final tongue length expected in the absence of gas leakage, t_0 the time at which the pressure was applied, τ_M the characteristic relaxation time of the compressible GV (Eq. **15**), and $\dot{L}_\infty$ the aspiration velocity in the pipette.

We also observed on many occasions that GV prepared with an initial protein concentration of 0.067 mg mL^{-1} presented a fragmentation of their tongue in the pipette during their aspiration (*SI Appendix*, Fig. S7). That phenomenon is called budding. It has been mentioned for GUVs and polymer-coated bubbles and is known to be caused by the minimization of the bending energy (48, 49).

Role of Compressibility. With the fit $L(t)$, we can obtain the value of L_e, which leads to a derivation of the dilatation modulus E_d^*. According to Eq. **14**, L_e is given by the classical model for incompressible capsules with an effective dilatation modulus $E_{d\,eff}^* = \frac{R_0^2(\Delta P - \Delta P_c)}{L_e\left(1 - \frac{R_p}{R}\right)}$. We find average values of 0.18 N m^{-1} (from 0.01 to 0.91 N m^{-1}, n = 22) and 0.32 N m^{-1} (from 0.14 to 1.38 N m^{-1}, n = 18) for liquid-like and glassy bubbles, respectively.

From $E_{d\,eff}^*$, according to Eq. **14**, we can derive the elastic modulus $E_d^* = \frac{E_{d\,eff}^*}{1 - \frac{4E_{d\,eff}^*}{3R_0P_e}}$, that is larger than $E_{d\,eff}^*$, with average values E_d^* of 0.24 N m^{-1} (from 0.01 to 1.87 N m^{-1}, n = 22, Fig. 6*A*) and 0.40 N m^{-1} (from 0.16 to 1.92 N m^{-1}, n = 18, Fig. 6*A*). With these values of E_d^*, we can estimate the increase ΔL_e of the tongue due to the compressibility from Eq. **14**. $\frac{\Delta L_e}{L_e} \cong \frac{4E_d^*}{3R_0P_e} \sim 0.09$ for liquid GV and 0.16 for glassy GV, which shows that the compressibility should be considered. This is due to the high rigidity of the coating, giving rise to a large membrane tension compressing the bubble.

The values of E_d^* are high, but it makes sense giving the high pressures of at least 12 kPa needed to aspirate the GV. We can notice that a few articles reporting elastic properties of similar systems are comparable to ours. First, millimetric bubbles coated with HFBII were found to have an area compression modulus evolving between 0.16 and 2 N m^{-1} using wrinkle analysis of a pendant capsule (analysis based on the formation of wrinkles on the surface of the protein membrane as the capsule is deflated) (29). Second, the surface expansion modulus of polymer-coated air bubbles has been reported using the classical model for incompressible systems (49). Depending on the polymer used, values from 0.075 to 0.65 N m^{-1} have been reported which are also quite similar to those presented in our work. Finally, HFBI monolayers at air/water interface have been studied using the surface shear rheology, and a surface shear elasticity G' equal to 0.7 N m^{-1} has been determined (17).

With E_d^* and the characteristic time τ_M found using the fit, we determine an average surface viscosity η_s of 3.2 mN s m^{-1} for liquid-like bubbles (from 0.06 to 8.7 mN s m^{-1}, n = 22, Fig. 6*B*) and 8.9 mN s m^{-1} for glassy bubbles (from 0.4 to 24.9 mN s m^{-1}, n = 18, Fig. 6*B*) using the equation $\eta_s = \frac{E_{d\,eff}^*\,\tau_M R_p^2}{4R_0^2\left(1 + \frac{R_p}{R}\right)}$. Since we determined the thickness of the hydrophobin membrane, we can approximate a bulk rigidity and a bulk viscosity. Considering the membrane thickness e = 2.7 ± 0.4 nm (n = 8) determined by cryo-TEM, we obtain rigidities $E = E_d^*/e \sim$ 8.9 10^7 Pa and 1.5 10^8 Pa, as well as bulk viscosities $\eta = \eta_s / e \sim$ 1.2 10^6 Pa s and 3.3 10^6 Pa s for liquid-like and glassy GV, respectively. By comparison, we have

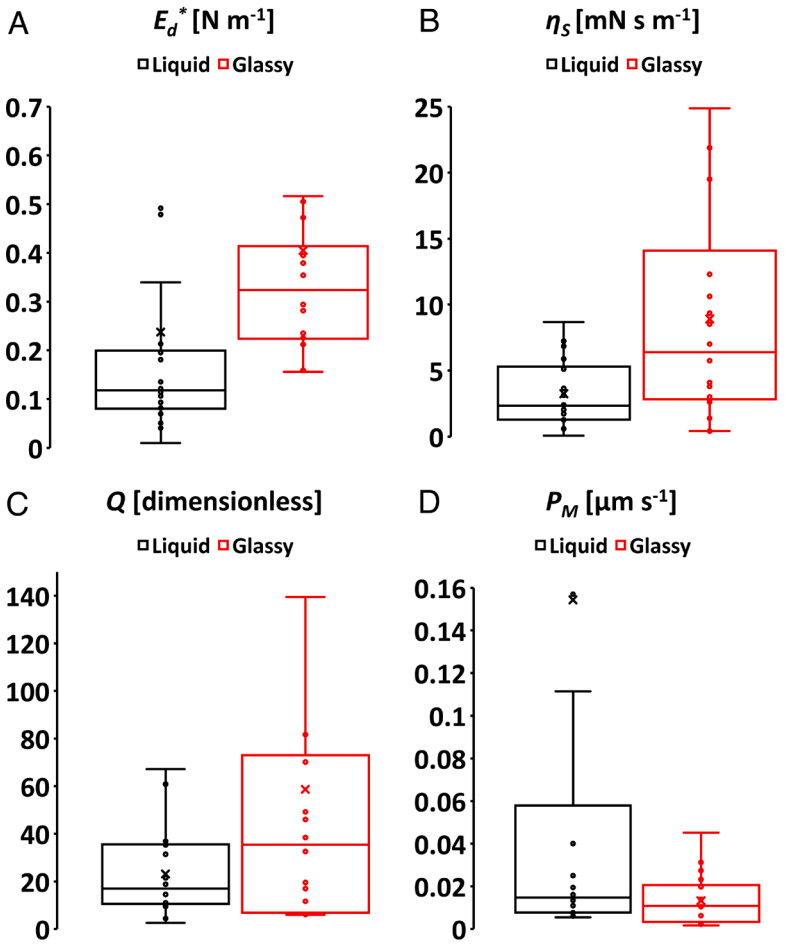

Fig. 6. Main characteristics of the liquid-like and glassy GV calculated using the pipette aspiration technique. (*A*) Elastic modulus E_d^* (n = 22 for liquid-like GV and n = 18 for solid-like GV), (*B*) surface viscosity η_S (n = 22 and 18), (*C*) sealing parameter Q (n = 18 and 18), and (*D*) permeability P_M (n = 18 and 18). For the sake of visualization, the two highest P_M points for liquid-like GV are not represented.

E_d^* (glassy) = 1.7 E_d^* (liquid) and η_s (glassy) = 2.8 η_s (liquid). These results indicate significantly higher mechanical properties of glassy GV compared to the liquid-like one, which can be explained if we consider that glassy GV have a denser protein network than their liquid-like counterpart. This is in agreement with the higher coating density of glassy GV.

For comparison, our average values of η_s are similar to that of giant liquid crystal polymersomes using the micropipette aspiration technique where 4.0 and 7.9 mN s m^{-1} have been found (50). Also, Cox et al. reported surface shear viscosities G'' = 0.2 N m^{-1} (for 7.5 10^{-2} mg mL^{-1} and ω = 1 Hz) and 0.04 N m^{-1} (for 0.75 mg mL^{-1} and ω = 1 Hz) that are 1 order higher than our values (17).

Permeation of GV. Measuring the aspiration velocity $\dot{L}_\infty$, the micropipette aspiration technique allows us to determine the permeation of gas across hydrophobin membranes. This method is convenient because it can be determined along with E_d^* and η_s and does not require additional experiments.

As demonstrated previously, the permeation parameter can be determined using Eq. **26** $\dot{L}_\infty = \frac{4P_M v_0(\Delta P - \Delta P_c)}{kT}$ assuming Q >1, where v_0 is the volume of a gas molecule inside the bubble. If we approximate the C_4F_{10} volume to 35 nm^3 (ρ = 11.21 kg m^{-3} and M_w = 238.028 g mol^{-1}), we obtain average permeabilities of 1.5 10^{-7} m s^{-1} for liquid-like GV (from 5.5 10^{-9} to 1.9 10^{-6} m s^{-1}, n = 18, Fig. 6*D*) and 1.3 10^{-8} m s^{-1} for glassy GV (from 1.6 10^{-9} to 4.5 10^{-8} m s^{-1}, n = 18, Fig. 6*D*). It shows that liquid GV are more permeable than glassy GV as expected by our model on the dynamics of protein adsorption. In comparison with the literature, our average values are three to four orders of magnitude lower to that obtained for vesicles with aquaporin pores (6.6 10^{-5} ± 1.5 10^{-5} m s^{-1}) (51). It is also equivalent to the porosity of (liquid-filled) polymersomes where the porosity varies mainly between 10^{-9} and 10^{-6} m s^{-1} depending on the systems studied (50, 52, 53). Considering that polymersomes are usually made of several layers of charged polyelectrolyte while in our case the membrane is made of a single layer of protein, it means that our protein membrane has a pretty good impermeability, which is very interesting considering the echogenic applications we are aiming at. The sealing parameter can be determined using Eq. **14.** $Q = \frac{R_p^2 kT}{P_M 16 v_0 \eta_s}$ We obtain average values of 23.1 for liquid-like GV (from 2.6 to 67.1, n = 18, Fig. 6*C*) and 58.7 for glassy GV (from 5.9 to 249, n = 18, Fig. 6*C*). These values, significantly higher than 1, confirm that we are working with a weakly permeable system and that we used the good formula to determine P_M and then Q. By comparison, we find P_M (glassy) = 0.09 P_M (liquid) and Q (glassy) = 2.5 Q (liquid). It tends to indicate that glassy GV are less permeable than the liquid-like ones, which again makes sense if we consider that glassy GV have an increased density at the interface compared to the liquid-like ones.

To check the model of permeation, we vary the medium viscosity and aspirate GV either in distilled water or a glycerol solution (50% w/w in distilled water). We measure the viscosity of distilled water

and the glycerol solution, and we obtain values of η_{water} = 0.92 mPa s and $\eta_{glycerol}$ = 6.5 mPa s (*SI Appendix*) leading to 7.1 η_{water}= $\eta_{glycerol}$. We determine the permeability from the velocity of extrusion given by Eq. **26**. The average value of P_M is 2.9 10^{-9} m s^{-1} (from 1.6 10^{-9} to 5.2 10^{-9} m s^{-1}, n = 9) and is significantly lower than the median value obtained in distilled water.

Since $P_M = \frac{na^3kT}{3\eta_L A v_0}$, we expect to obtain values of P_M that about 7 times higher in water than in the glycerol solution. We found P_M *(water, liquid) = 52* P_M *(glycerol) and* P_M *(water, glassy) = 5* P_M *(glycerol)*. This decrease of the permeability in glycerol confirms our model and is strongest than expected, which may be explained by a modification of the protein coating in glycerol.

Materials and Methods

Materials. HFBI hydrophobin protein is produced and purified as described in Linder et al. (21) C_4F_{10} 98% (CAS 355-25-9) was purchased from ABCR (Karlsruhe, Germany). Water was purified using a Milli-Q system (Millipore) with resistivity around 18.2 MΩ cm.

Formation of Bubbles. The bubbles used in this study were created by a mechanical agitation method. The desired amount of HFBI (0.02, 0.067, or 0.2 mg) was solubilized in 1 mL of phosphate buffer saline (1×) placed inside a 2.5 mL glass vial. The vial was sealed using an aluminum cap and a septum, and the air inside was replaced with C_4F_{10} using a 50 mL Hamilton syringe. The vial was placed in a VialMix shaker (Lantheus) and agitated for 45 s, forming a white-colored suspension consisting of micro- and nanobubbles (*SI Appendix*, Fig. S1).

Cryo-TEM. A 5 μL droplet of nanosized bubble dispersion was deposited onto a plasma-treated lacey carbon-coated copper grid (Electron Microscopy Sciences). The droplet was blotted with filter paper, plunged into liquid ethane (−170 °C) using an automatic plunge freezer (EM GP2, Leica), and stored in liquid nitrogen. The samples were inspected using a JEM-3200FSC (JEOL) microscope with an accelerating voltage of 300 kV, and images were acquired using Digital Micrograph software (Gatan, version 1.83.842).

AFM. The AFM measurements were carried out using a Dimension Icon AFM (Bruker AXS, France; formerly Veeco) with ScanAsyst-air cantilevers (sharp silicon nitride tips with a nominal radius of 2 nm for PeakForce Tapping in air). The scan size was set to 100 nm × 100 nm with a resolution of 256 pix × 256 pix, and the scanning was performed with a scan rate of 1 kHz. ScanAsyst Auto control was set to "individual" for the sample with PeakForce Amplitude of 170 nm. The spring constant and peak force frequency were 0.4 N m^{-1} and 2 kHz for all samples. Individual scans for each sample were taken at multiple locations on the surface.

Sample Preparation for AFM. A 100 mL droplet of HFBI solution (0.2 mg mL^{-1}) was placed on a parafilm substrate for about 1 h to get a flattened area on the top of the droplet and confirm that we had a monolayer at the interface. After that, a highly ordered pyrolytic graphite substrate was brought into contact with the top of the droplet. The substrate with the hydrophobin monolayer was gently washed with 200 mL of Milli-Q water. The sample was placed on the AFM stage, and we waited for about 30 min to ensure that the sample was dry. Finally, the sample was imaged. *SI Appendix*, Fig. S2 shows the sample preparation procedure.

Surface Tension and Surface Dilatational Rheology. Measurements of the surface tension and mechanical properties of the HFBI adsorbed layer were carried out using an optical tensiometer (Theta tensiometer, Biolin Scientific, Finland), and the obtained data were analyzed using the instrument software (OneAttension). A hooked needle filled with C_4F_{10} using a Hamilton syringe was immersed in a solution of HFBI (0.01 mg mL^{-1}). Then, a 10 μL gas bubble was created on the needle tip, and the bubble was monitored for about 3 h until the surface tension curvature reached a steady state. At that point, the static surface tension was measured by applying a sinusoidal volume disruption using an integrated pulsated droplet module (PD-200, Biolin Scientific, Finland). The change in bubble volume was monitored for 40 s (*SI Appendix*, Table S2).

Density and Viscosity Measurements. Density measurements of distilled water (as a reference) and a glycerol solution (50% w/w in distilled water) were performed in triplicate using a handheld density meter (Mettler Toledo, DensitoPro model) (*SI Appendix*, Table S3).

The viscosity of these solutions was then measured using a homemade setup consisting of a piezoelectric pressure controller (OB1 Mk3, Elveflow) connected to a balance via a reservoir. The reservoir was filled with the solution to be characterized and connected to the balance via a tubing inside a glass vial placed on the balance. The flow rate Q of the liquid was deduced by observing the increase in mass of the vial after a 30 s increase in pressure in the reservoir and using the density of the solution. Pressures of 125 Pa were applied for distilled water and 500 Pa for the glycerol solution using Elveflow pressure controller (software ESI v3.06.05). Measurements were performed at room temperature (T = 23 ± 1 °C) and were repeated 15 times for each solution. The flow rate was then used to determine the viscosity of the solution using the Hagen–Poiseuille equation

$$\eta_L = \frac{\Delta P \pi r^4}{8LQ},$$

where ΔP is the applied pressure, r is the radius of the tubing, and L is the length of the tubing (*SI Appendix*, Table S4).

Pipette Aspiration Setup and Microscopy. Micropipettes were prepared by pulling borosilicate capillaries (WPI, 1 mm/0.5 mm outer/inner diameter) using a puller (PN-31, Narishige). Afterward, the micropipettes were sized to a few micrometers in diameter and bent using a microforge (MF-900, Narishige) to introduce the pipette horizontally in the observation chamber. The pipette was connected through tubing to a water tank attached to the piezoelectric pressure controller mentioned previously and then filled with water. The observation chamber was made of two glass coverslips separated with a few layers of parafilm and was filled with the solution containing the bubbles. The micropipette was brought into contact with a GGV (HFBI-coated microbubble) and a negative pressure was applied, resulting in the suction of the microbubble with the formation of a tongue of length $L(t)$. The experiments were performed at room temperature (T = 23 ± 1 °C), and aspirated microbubbles were visualized with an inverted microscope (Nikon Eclipse Ti). Bright-field images were recorded with a sCMOS camera (Zyla-4.2-CL10, Andor) at a time interval between 0.2 and 1 s and operated using μManager (2.0 beta) open-source microscopy software (*SI Appendix*, Table S1 and S5).

Conclusion

The mechanical properties and stability of GV are crucial as they play a fundamental role in therapeutic and diagnostic techniques as contrast agents for ultrasound imaging. In addition, they can be used as a drug and oxygen cargo for therapy. It has also been shown that they can serve as agents for cell destruction and tissue disruption through ultrasound-induced inertial cavitation (54). This property is enabled by GV produced by bacteria, which are protein nanostructures filled with gas to achieve cellular buoyancy. They have given rise to bacterial therapies since the genes that encode GV can be expressed in mammalian cells. The GGV studied here are not protein nanostructures but microstructures, which allows to study their mechanical properties. It will also be interesting to form GV with proteins from bacteria.

We have demonstrated that the hydrophobin-coated bubbles formed here have improved mechanical properties, which will enable them to be used for echogenic applications. Their stability is ensured by the adsorption of proteins at the liquid–gas interface. This surface film can be in the liquid or solid state depending on the amount of hydrophobin adsorbed at the interface. In the first case, the surface tension can be measured by the hanging drop technique by analyzing its shape. Alternatively, the response of the surface tension $\sigma(V, \omega)$ to a periodic modulation of the volume of the bubble can be measured. This allows to highlight the viscoelastic properties of the surface film from the phase shift between the volume change and the response of the protein film tension.

We show here that the micropipette aspiration technique is the most efficient because it allows the study of GV in both liquid and glassy states. If the film is glassy, it presents a transition to a liquid state if a stress higher than a yield stress is applied to it. It corresponds to a threshold suction pressure above which the GV enters the pipette in a liquid state, forming a sleeve that adapts the shape of the pipette. In all cases, the vesicles penetrate only if ΔP is larger than the Laplace threshold $\Delta P_C(\sigma_0)$. Contrary to the suction of simple bubbles or liquid drops, the GV penetrates only partially because the membrane tension increases with the size of the sleeve, and the penetration stops when $\Delta P = \Delta P_C(\sigma_e)$. In the glassy case, the tongue penetration is achieved if both conditions (σ larger

than the yield stress and the aspiration Laplace pressure threshold) are met. When the aspiration is stopped, the sleeve becomes glassy again and keeps its shape. It can be resorbed by sucking the deformed vesicle beyond the yield stress. We have discovered a new regime where a very long tongue is formed at ultra-fast velocity. It corresponds to the aspiration of gas from the glassy vesicles. In this case, the stress σ acting on the protein shell is smaller than the yield stress and larger than the Laplace pressure to aspirate a bubble of gas. This extraction of gas from solid GV may have applications in ultrasound-induced inertial cavitation.

GGV aspiration was modeled by introducing both gas compressibility and film permeability. We demonstrate that compression leads to an increase in tongue penetration $\frac{\Delta L_e}{L_e} \cong \frac{4E_d^*}{3R_0P_e}$ of the order of 12%, which is not negligible due to the high value of the dilatation modulus E_d^*. In addition, membrane permeability gives rise to new laws relating the membrane tension to the applied pressure.

Thanks to the model, we were able to measure the static and dynamic properties of the interfacial film: its elastic stretch modulus, its viscosity, and its porosity.

We have shown that the membrane tension σ is not always given by the Laplace formula relating the tension ΔP to σ and the pipette radius R_p. We defined the sealing parameter Q that separates two regimes of low and high porosity, where the bubble tension almost vanishes in the steady-state regime. It would be interesting to investigate the case of more porous systems, either by varying the mesh size of the surface protein network, or by looking at the case of Pickering bubbles where the pores have sizes comparable to the size of the particles adsorbed at the interface.

Finally, the mechanical properties we were able to measure indicate that the GV developed in this project can be used as a multifunctional platform for both targeting for molecular imaging and for drug delivery after modification of the shell with specific targeting agents.

Data, Materials, and Software Availability. All study data are included in the article and/or *SI Appendix*.

ACKNOWLEDGMENTS. This work was carried out under the Academy of Finland Center of Excellence Program (2022-2029) in Life-Inspired Hybrid Materials (LIBER) (project numbers 346109 and 346112). The authors acknowledge the provision of facilities and technical support by Aalto University at OtaNano Nanomicroscopy Center (Aalto-NMC) and Pascal Hersen for stimulating discussions on gas vesicles.

Author affiliations: [a]Department of Applied Physics, Aalto University School of Science, Espoo, Aalto FI-00076, Finland; [b]VTT Technical Research Centre of Finland Ltd., Espoo, FI-02044 VTT, Finland; [c]Institut Curie, Université Paris Sciences et Lettres, Sorbonne Université, CNRS UMR168, Laboratoire Physico Chimie Curie, Paris 75005, France; and [d]Department of Bioproducts and Biosystems, Aalto University School of Chemical Engineering, Espoo, Aalto FI-00076, Finland

1. A. Bar-Zion *et al.*, Acoustically triggered mechanotherapy using genetically encoded gas vesicles. *Nat. Nanotechnol.* **16**, 1403–1412 (2021), 10.1038/s41565-021-00971-8.
2. R. Smith-Bindman *et al.*, Trends in use of medical imaging in US health care systems and in Ontario, Canada, 2000–2016. *JAMA* **322**, 843–856 (2019).
3. Operational Information for Commissioning, "Diagnostic imaging dataset annual statistical release 2017/18" (Tech. Rep. Ser. No. 1.0, NHS England, Leeds, UK, 2018).
4. P. Frinking, T. Segers, Y. Luan, F. Tranquart, Three decades of ultrasound contrast agents: A review of the past, present and future improvements. *Ultrasound Med. Biol.* **46**, 892–908 (2020).
5. G. Köse, M. Darguzyte, F. Kiessling, Molecular ultrasound imaging. *Nanomaterials* **10**, 1935 (2020).
6. A. De Leon *et al.*, Contrast enhanced ultrasound imaging by nature-inspired ultrastable echogenic nanobubbles. *Nanoscale* **11**, 15647–15658 (2019).
7. M. S. Khan *et al.*, Oxygen-carrying micro/nanobubbles: Composition, synthesis techniques and potential prospects in photo-triggered theranostics. *Molecules* **23**, 1–19 (2018).
8. A. L. Emanuel *et al.*, Contrast-enhanced ultrasound for quantification of tissue perfusion in humans. *Microcirculation* **27**, e12588 (2020).
9. B. Ihnatsenka, A. P. Boezaart, Ultrasound: Basic understanding and learning the language. *Int. J. Shoulder Surg.* **4**, 55–62 (2010).
10. J. G. Riess, Understanding the fundamentals of perfluorocarbons and perfluorocarbon emulsions relevant to in vivo oxygen delivery. *Artif. Cells, Blood Substitutes, Immobilization Biotechnol.* **33**, 47–63 (2005).
11. L. Gazzera *et al.*, Design of highly stable echogenic microbubbles through controlled assembly of their hydrophobin shell. *Wiley Online Library* **55**, 10263–10267 (2016).
12. W. Kloek, T. Van Vliet, M. Meinders, Effect of bulk and interfacial rheological properties on bubble dissolution. *J. Colloid Interface Sci.* **237**, 158–166 (2001).
13. E. Evans, D. Needham, Physical properties of surfactant bilayer membranes: Thermal transitions, elasticity, rigidity, cohesion and colloidal interactions. *J. Phys. Chem.* **91**, 4219–4228 (1987).
14. J. G. H. Wessels, Hydrophobins, unique fungal proteins. *Mycologist* **14**, 153–159 (2000).
15. A. Walther, A. H. E. Müller, Janus particles. *Soft Matter* **4**, 663 (2008).
16. J. G. H. Wessels, O. M. H. De Vries, S. A. Asgeirsdottir, F. H. J. Schuren, Hydrophobin genes involved in formation of aerial hyphae and fruit bodies in Schizophyllum. *The Plant cell* **3**, 793–799 (1991).
17. A. R. Cox, F. Cagnol, A. B. Russell, M. J. Izzard, Surface properties of class II hydrophobins from Trichoderma reesei and influence on bubble stability. *Langmuir* **23**, 7995–8002 (2007).
18. H. A. B. Wosten, O. M. H. De Vries; J. G. H. Wessels' Department, Interfacial self-assembly of a fungal hydrophobin into a hydrophobic rodlet layer. *Am. Soc. Plant Physiol.* **5**, 1567–1574 (1993).
19. M. B. Linder, Hydrophobins: Proteins that self assemble at interfaces. *Curr. Opin. Colloid Interface Sci.* **14**, 356–363 (2009).
20. M. Linder *et al.*, The hydrophobins HFBI and HFBII from Trichoderma reesei showing efficient interactions with nonionic surfactants in aqueous two-phase systems. *Biomacromolecules* **2**, 511–517 (2001).
21. G. R. Szilvay *et al.*, Self-assembled hydrophobin protein films at the air-water interface: Structural analysis and molecular engineering. *Biochemistry* **46**, 2345–2354 (2007).
22. A. Paananen *et al.*, Structural hierarchy in molecular films of two class II hydrophobins. *Biochemistry* **42**, 5253–5258 (2003).
23. R. Y, L. Boruvka, A. W. Neumann, Determination of surface tension and contact angle from the shapes of axisymmetric fluid interfaces. *J. Colloid Interface Sci.* **93**, 169–183 (1983).
24. O. I. del R. and A. W. Neumann, Axisymmetric drop shape analysis: Computational methods for the measurement of interfacial properties from the shape and dimensions of pendant and sessile drops. *J. Colloid Interface Sci.* **196**, 136–147 (1997).
25. M. Hoorfar, A. W. Neumann, Recent progress in axisymmetric drop shape analysis (ADSA). *Adv. Colloid Interface Sci.* **121**, 25–49 (2006).
26. J. D. Berry, M. J. Neeson, R. R. Dagastine, D. Y. C. Chan, R. F. Tabor, Measurement of surface and interfacial tension using pendant drop tensiometry. *J. Colloid Interface Sci.* **454**, 226–237 (2015).
27. S. R. Derkach, J. Krägel, R. Miller, Methods of measuring rheological properties of interfacial layers (Experimental methods of 2D rheology). *Colloid J.* **71**, 1–17 (2009).
28. A. W. Adamson, *Physical Chemistry of Surfaces, 6th Edition* (John Wiley & Sons, Inc., 1997).
29. S. Knoche *et al.*, Elastometry of deflated capsules: Elastic moduli from shape and wrinkle analysis. *Langmuir* **29**, 12463–12471 (2013).
30. M. Sato, D. P. Theret, L. T. Wheeler, N. Ohshima, R. M. Nerem, Application of the micropipette technique to the measurement of cultured porcine aortic endothelial cell viscoelastic properties. *J. Biomech. Eng.* **112**, 263–268 (1990).
31. E. Evans, B. Kukan, Passive material behavior of granulocytes based on large deformation and recovery after deformation tests. *Blood* **64**, 1028–1035 (1984).
32. R. M. Hochmuth, Micropipette aspiration of living cells. *J. Biomech.* **33**, 15–22 (2000).
33. K. Guevorkian, M. -J. Colbert, M. Durth, S. Dufour, F. Brochard-Wyart, Aspiration of Biological Viscoelastic Drops. *Phys. Rev. Lett.* **104**, 218101 (2010).
34. K. Guevorkian, J. Manzi, L.-L. Pontani, F. Brochard-Wyart, C. Sykes, Mechanics of biomimetic liposomes encapsulating an actin shell. *Biophys. J.* **109**, 2471–2479 (2015).
35. E. Evans, W. Rawicz, Entropy-driven tension and bending elasticity in condensed-fluid membranes. *Phys. Rev. Lett.* **64**, 2094–2097 (1990).
36. L. Lu, W. J. Doak, J. W. Schertzer, P. R. Chiarot, Membrane mechanical properties of synthetic asymmetric phospholipid vesicles. *Soft Matter* **12**, 7521–7528 (2016).
37. Z. Kang, A. Yeung, J. M. Foght, M. R. Gray, Hydrophobic bacteria at the hexadecane–water interface: Examination of micrometre-scale interfacial properties. *Colloids Surf. B* **67**, 59–66 (2008).
38. A. Yeung, T. Dabros, J. Masliyah, J. Czarnecki, Micropipette: A new technique in emulsion research. *Colloids Surf. A* **174**, 169–181 (2000).
39. A. B. Pawar, M. Caggioni, R. Ergun, R. W. Hartel, P. T. Spicer, Arrested coalescence in Pickering emulsions. *Soft Matter* **7**, 7710 (2011).
40. G. Kaufman *et al.*, Soft microcapsules with highly plastic shells formed by interfacial polyelectrolyte–nanoparticle complexation. *Soft Matter* **11**, 7478–7482 (2015).
41. N. Samudrala, J. Nam, R. Sarfati, R. W. Style, E. R. Dufresne, Mechanical stability of particle-stabilized droplets under micropipette aspiration. *Phys. Rev. E* **95**, 012805 (2017).
42. E. Mabrouk *et al.*, Formation and material properties of giant liquid crystal polymersomes. *Soft Matter* **5**, 1870 (2009).
43. N. P. Kamat, M. H. Lee, D. Lee, D. A. Hammer, Micropipette aspiration of double emulsion-templated polymersomes. *Soft Matter* **7**, 9863 (2011).
44. K. Olbrich, W. Rawicz, D. Needham, E. Evans, Water permeability and mechanical strength of polyunsaturated lipid bilayers. *Biophys. J.* **79**, 321–327 (2000).
45. W. Rawicz, B. A. Smith, T. J. McIntosh, S. A. Simon, E. Evans, Elasticity, strength, and water permeability of bilayers that contain raft microdomain-forming lipids. *Biophys. J.* **94**, 4725–4736 (2008).
46. D. H. Kim, M. J. Costello, P. B. Duncan, D. Needham, Mechanical properties and microstructure of polycrystalline phospholipid monolayer shells: Novel solid microparticles. *Langmuir* **19**, 8455–8466 (2003).
47. J. Happel, H. Brenner, *Low Reynolds Number Hydrodynamics* (Springer, Dordrecht, ed. 1, 1983).
48. U. Seifert, R. Lipowsky, Adhesion of vesicles. *Phys. Rev. A* **42**, 4768–4771 (1990).
49. Y. Jang *et al.*, Tuning the mechanical properties of recombinant protein-stabilized gas bubbles using triblock copolymers. *ACS Macro Lett.* **5**, 371–376 (2016).
50. A. A. Antipov, G. B. Sukhorukov, Polyelectrolyte multilayer capsules as vehicles with tunable permeability. *Adv. Colloid Interface Sci.* **111**, 49–61 (2004).
51. A. Berthaud *et al.*, Spreading of porous vesicles subjected to osmotic shocks: The role of aquaporins. *Soft Matter* **12**, 1601–1609 (2016).
52. G. Ibarz, L. Dähne, E. Donath, H. Möhwald, Controlled permeability of polyelectrolyte capsules via defined annealing. *Chem. Mater.* **14**, 4059–4062 (2002).
53. K. Kono, F. Tabata, T. Takagishi, pH-responsive permeability of poly(acrylic acid)–poly(ethylenimine) complex capsule membrane. *J. Membrane Sci.* **76**, 233–243 (1993).
54. M. G. Shapiro *et al.*, Biogenic gas nanostructures as ultrasonic molecular reporters. *Nat. Nanotech* **9**, 311–316 (2014).